

A Parallel Excitation Based Fluorescence Molecular Tomography System for Whole-Body Simultaneous Imaging of Small Animals

FEI LIU, XIN LIU, DAIFA WANG, BIN ZHANG, and JING BAI

Department of Biomedical Engineering, School of Medicine, Tsinghua University, Beijing 10084, China

(Received 23 March 2010; accepted 30 May 2010; published online 11 June 2010)

Associate Editor Daniel Elson oversaw the review of this article.

Abstract—Challenges remain in imaging complete dynamic physiological processes *in vivo* through the whole small animal body using fluorescence molecular tomography (FMT). In this article, a novel non-contact full-angle FMT system that enables whole-body simultaneous imaging of small animals is presented. The whole-body simultaneous imaging ability is achieved by employing a line-shaped parallel excitation source, which can provide extended spatial sampling dataset to reconstruct multiple fluorescent targets distributed in whole animal body during one full-angle FMT imaging process. The key performances of this system were evaluated by a series of experiments. Quantitation linearity for over two orders of magnitude of fluorescence markers concentration was demonstrated, and an accessible simultaneous imaging domain of $4.0 \times 1.5 \text{ cm}^2$ could be achieved utilizing the parallel excitation pattern. Moreover, the *in vivo* imaging feasibility and performance were validated by localizing two fluorescent targets implanted at different positions of a nude mouse. The results suggest that compared with conventional single point excitation FMT system, the proposed system can achieve a whole-body simultaneous imaging domain and impart the ability to image complete dynamic physiological processes *in vivo*.

Keywords—Fluorescence molecular tomography, Image reconstruction techniques, Medical and biological imaging.

INTRODUCTION

Fluorescence molecular tomography (FMT) is a newly emerged technology directed toward noninvasive, quantitative, three-dimensional (3D) imaging of internal distribution of fluorescence markers *in vivo*.^{16,21,22} It opens an exciting route to 3D imaging and visualization of disease pathogenesis,^{2,4,8,9,24} drug development,²⁸ and therapeutic response^{19,20,23} in small animals.

During the last decade, FMT systems have been evolved over several generations. The early fiber-based FMT system suffers from a compromised dataset and a highly ill-posed inverse problem due to the small number of optical fibers employed.²⁵ A mechanical raster scanning based parallel-plate (slab) imaging geometry is developed to achieve a higher spatial photon sampling. However, it still has compromised resolution along the axis perpendicular to the detector plane due to the limited projection angles.^{7,27} Besides, in order to minimize photon wave mismatches, matching fluids are utilized in these two types of systems, which add complexity and instability to the setup. Recent advance in FMT is the non-contact full-angle tomography system. It can achieve high spatial sampling of photons propagating through tissue offered by full-angle projection measurements and simplify experimental setups since no matching fluids are utilized and no fibers are brought in to contact with the imaged object.^{3,10,17} However, optical fibers or laser beams employed in these systems as the light source mainly work in a point excitation pattern, which can only excite a limited volume and acquire fluorescent signals from a local region of the animal body. Fluorescent targets distributed in other volumes of interest may be potentially missed. As a result, the studies of non-contact full-angle FMT in small animal imaging are limited to a local region, such as the mouse lungs,² spleen,⁵ brain,¹¹ thymus,¹⁷ respectively, and the applications in imaging whole-body fluorescent targets distributions have been restricted. To provide a whole-body simultaneous imaging performance in non-contact full-angle FMT system, a kind of parallel excitation pattern including line excitation and area excitation has been proposed by Wang *et al.*³³ In their reports, they mainly focused on the theoretical analysis of optimal imaging parameters of FMT. Although it was helpful in guiding the design of FMT system with

Address correspondence to Jing Bai, Department of Biomedical Engineering, School of Medicine, Tsinghua University, Beijing 10084, China. Electronic mail: deabj@tsinghua.edu.cn

parallel excitation, most of the work was conducted under numerical simulation studies.

In this article, we implement a FMT system designed for imaging whole-body distribution of fluorescent markers in small animals based on a line-shaped parallel excitation pattern. The parallel excitation pattern can excite an extended domain on the imaged object and then provide extended spatial sampling dataset to reconstruct multiple fluorescent targets distributed in whole animal body simultaneously during one full-angle FMT imaging process. The fluorescent marker we employed, indocyanine green (ICG), is a widely used optical fluorophore in the near-infrared (NIR) range for small animal^{1,35} and human cancer imaging.^{6,14,18} A series of phantom experiments were performed to evaluate the key parameters of this system. The capacity of quantitation linearity was assessed with glass tube containing different ICG concentrations in a cylinder phantom. The accessible simultaneous imaging domain was illustrated by two fluorescent tubes placed at different positions of the glass cylinder. Furthermore, animal experiment with two fluorescent targets implanted in the torso of a nude mouse was conducted to demonstrate the performance of this system to localize and quantify whole-body fluorescent distributions *in vivo*. The experimental results suggest that the proposed system can achieve a whole-body simultaneous imaging domain and has the advantage of imaging complete dynamic physiological processes *in vivo* compared with conventional single point excitation FMT system.

This article is structured as follows: we first give a detailed description of the system setup and a brief

introduction to the reconstruction algorithm. Then the key performances of this system are evaluated by a series of phantom and *in vivo* experiments. Finally, the major advantage, application potential of the proposed system and future work are discussed.

MATERIALS AND METHODS

Experimental Setup

We have developed a non-contact full-angle FMT system for simultaneous imaging of whole-body distribution of fluorescent markers in small animals. The system mainly contains three modules, as shown in Fig. 1.

The Excitation Module

The excitation module consists of the light source, the excitation filter, and the excitation fiber. A 250 W Halogen lamp (i) (7ILT250, 7-star, Beijing, China), with wavelength range from 300 to 2500 nm is employed as the excitation light source. Since ICG is employed as the fluorescent marker in the following studies, a band pass excitation filter (ii) (FF01-775/46-25, Semrock, Rochester, NY, USA) with a center wavelength of 775 nm, full width half maximum (FWHM) of 46 nm is used in front of the Halogen lamp. The excitation light which travels through the filter is coupled with a special optical fiber (iii), which is the core component of this system. One end of the fiber facing the Halogen lamp is circular in shape as usual,

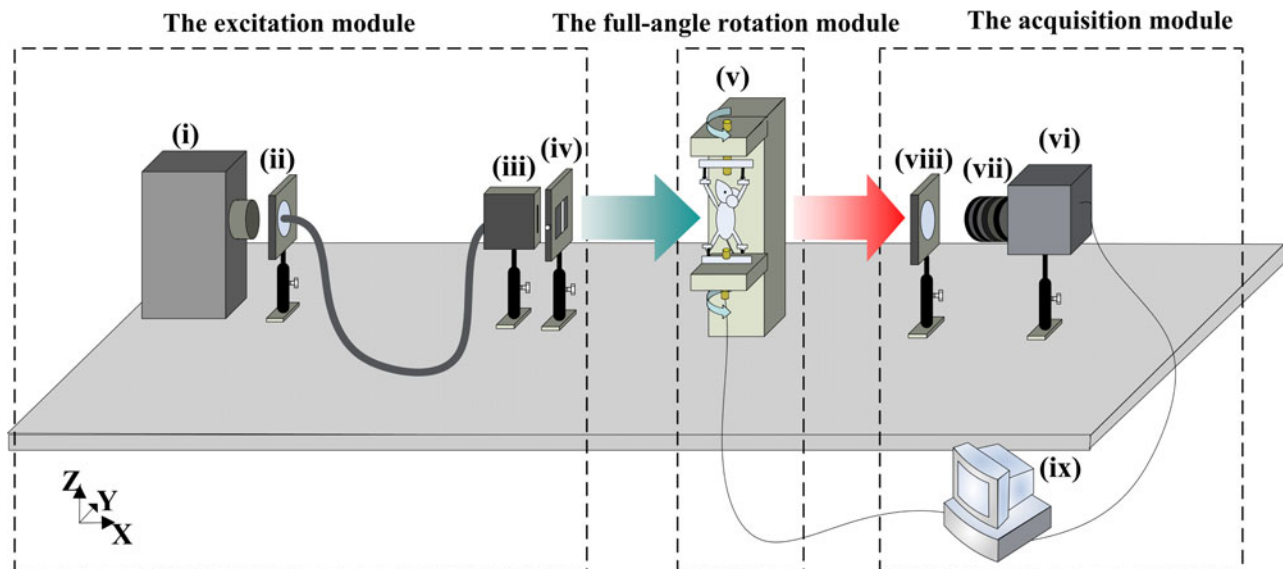


FIGURE 1. Experimental setup of the parallel excitation based FMT system.

while the other end toward the imaged object is rectangular in shape. The output of the rectangular end is a line-shaped beam along Z axis. The line-shaped excitation beam has a maximum length of 4 cm and the light intensity distribution along the length of the beam is designed to be uniform. An adjustable slit (iv) is used to control the width of the excitation beam and cut off light with large diverse angles.

The Full-Angle Rotation Module

Full-angle projection measurements are implemented by a 360° rotation stage (v). The imaged animal is suspended by a home-made holder, consists of four clips that fasten the animal's extremities and fix the animal onto the rotation stage. The stage allows rotation of the object around its longitudinal axis (Z axis) for full-angle projection acquisitions, with a resolution of 0.0025° and repeatability error $<0.01^\circ$. The rotation parameters such as speed, direction, and rotation steps can be manipulated by a motor controller. The typical rotation speed is set to $6^\circ/s$ to avoid skew and internal organs movement. The experimental animal is anesthetized by an isoflurane veterinary vaporizer (VMR, Matrx, NY, USA) during *in vivo* imaging process.

The Acquisition Module

The FMT data is acquired by a -70°C , high frame rate electron multiplying charge-coupled device (EMCCD) camera (vi) (iXon DU-897, Andor Technologies, Belfast, Northern Ireland) placed on the opposite side of the imaged object. A 60 mm f/2.8 imaging lens (vii) (Nikon, Melville, NY, USA) is coupled to EMCCD. For ICG fluorescence detection, a band pass emission filter (viii) (FF01-840/12-25, Semrock, Rochester, NY, USA) with a center wavelength of 840 nm, FWHM of 12 nm is employed in front of the EMCCD camera. Additional excitation and emission filter pairs for other fluorescent markers at different spectral bands have been added in this system but are not referred to herein.

The entire experimental procedure such as rotation control and data acquisition is manipulated by a 2.4 GHz 32 bit PC (ix) with self-designed software developed under the LABWINDOWS environment.

Imaging Protocol

In our experiment, the length of the line-shaped parallel excitation beam was set to 4 cm and the width of the excitation beam was set to about 0.1 cm, considering that the excitation light should be efficient enough to excite the whole imaged object while avoid

transmitting to CCD directly without interacting with the object. After fixing an imaged object on the rotation stage, full-angle FMT was performed with the rotation stage working under a step-by-step mode.

The fluorescence images were acquired typically utilizing 36 projections every 10° , with the corresponding filters mentioned in experimental setups. The excitation light images were acquired under the same conditions except for the fluorescence filter replaced by a neutral density filter (Daheng, Beijing, China) with 1% light transmittance for normalized Born approximation.³² 72 white light images were collected using an incandescent lamp instead of the excitation source, to recover the 3D surface of the imaged object.³⁴ The typical EMCCD field of view (FOV) was about $7 \times 7 \text{ cm}^2$ in this article.

Reconstruction Algorithm

FMT reconstruction is performed for localization and quantification of fluorescence markers in imaged object. In highly scattering tissue medium, the photon propagation can be modeled using the diffusion equation coupled with Robin-type boundary condition.³⁰ For a continuous wave (CW) source term $S(r)$, the Green's function $G(r)$, which describes the photon propagation field, can be presented as follows:

$$\begin{cases} -\nabla \cdot [D(r)\nabla G(r)] + \mu_a(r)G(r) = S(r) & r \in \Omega \\ 2qD(r)\frac{\partial G(r)}{\partial \vec{n}} + G(r) = 0 & r \in \partial\Omega \end{cases}, \quad (1)$$

where $D(r) = 1/(3\mu'_s(r))$ is the diffusion coefficient at position r . $\mu'_s(r)$ is the reduced scattering coefficient and $\mu_a(r)$ is the absorption coefficient. Ω is the domain of the imaged object with a boundary of $\partial\Omega$. q is a constant depending on the optical refractive index mismatch on the boundary and \vec{n} denotes the outward normal vector of the boundary $\partial\Omega$. A collimated point source spot can be modeled as an isotropic source $S(r) = \delta(r - r_s)$, where r_s is the point one transport mean free path $\text{ltr} = 1/\mu'_s(r)$ into the medium from the illumination spot.³⁰ In analogy, a uniform line-shaped excitation source term employed in the proposed system is modeled as:

$$L(r) := \begin{cases} L(r) = 1/L & r \in \{r_1\} \\ L(r) = 0 & r \notin \{r_1\} \end{cases}, \quad (2)$$

where $\{r_1\}$ denotes a line one transport mean free path into the medium from the central axis of the narrow beam with a length of L . In practical implementation, $L(r)$ is defined linear to intensity profile with $\int_{\{r_1\}} L(r)dr = 1$. If knowing the optical properties, the Green's function $G(r)$ can be obtained by solving Eq. (1) using finite element method.^{13,31} Given Green's

functions, the measured fluorescence signal at detector point r_d can be expressed as²⁶:

$$U_m(r_d) = \int_V G_{\delta(r-r_d)}^{\lambda_n}(r_p) n(r_p) \Phi_{\{r_1\}}^{\lambda_{exc}}(r_p) dr_p, \quad (3)$$

where r_p is the point inside the volume V considered for reconstruction. $n(r_p) = \eta \mu_{axf}(r_p)$ denotes the fluorescence yield at r_p , with η being the quantum efficiency and μ_{axf} being the absorption coefficient of the fluorophore. In general, the fluorescence yield is proportional to the fluorochrome concentration. $G_{\delta(r-r_d)}^{\lambda_n}(r_p)$ denotes the Green's function value at r_p due to a point source $\delta(r - r_d)$ at the fluorescence wavelength, and $\Phi_{\{r_1\}}^{\lambda_{exc}}$ denotes the spatial distribution of excitation light due to a line-shaped excitation source $L(r)$ along $\{r_1\}$. Assuming identical optical properties at both excitation and emission wavelength, the photon density $\Phi_{\{r_1\}}^{\lambda_{exc}}$ is modeled using the same Green's functions as U_m . The measured excitation signal at detector point r_d can be expressed as:

$$U_x(r_d) = G_{\{r_1\}}^{\lambda_{exc}}(r_d), \quad (4)$$

where $G_{\{r_1\}}^{\lambda_{exc}}(r_d)$ denotes the Green's function value at r_d due to a line-shaped excitation source $L(r)$ along $\{r_1\}$ at the excitation wavelength. To reduce the influence of tissue heterogeneity, normalized Born method is employed.³² By dividing Eq. (3) with Eq. (4), the normalized ratio $U_m(r_d)/U_x(r_d)$ of the measured fluorescence signal and corresponding excitation signal at detector point r_d can be expressed as follows:

$$\frac{U_m(r_d)}{U_x(r_d)} = \Theta \frac{\int_V G_{\delta(r-r_d)}^{\lambda_n}(r_p) n(r_p) G_{\{r_1\}}^{\lambda_{exc}}(r_p) dr}{G_{\{r_1\}}^{\lambda_{exc}}(r_d)}, \quad (5)$$

where the Green's function $G_{\{r_1\}}^{\lambda_{exc}}$ at the excitation wavelength has replaced $\Phi_{\{r_1\}}^{\lambda_{exc}}$ in Eq. (3), and a unitless calibration factor Θ is added to account for the amplification and attenuation factors of the system. When the volume V is discretized into voxels, a linear relation between the normalized vector U_m/U_x and the unknown fluorescence yield vector n is generated as follows:

$$\frac{U_m}{U_x} = \mathbf{W}n. \quad (6)$$

In the weight matrix \mathbf{W} , each element w_{ij} means the contribution of j th voxel of the discrete field of interest (FOI) to the measurement due to the i th source-detector pair. The unknown fluorescence yield vector n is reconstructed by solving the linear system using algebraic reconstruction technique (ART). In our studies, the reconstructions were terminated after 300 ART iterations. The actual computation time on our personal computer (Intel Core TMI5 processor and

8 GB RAM) for a weight matrix \mathbf{W} with 10^8 elements was approximate 1.1 min. As the computation time is linear to the number of elements in the weight matrix \mathbf{W} , for \mathbf{W} with other sizes, the computation time can be approximately estimated.

RESULTS

Quantification Linearity

A 2.5-cm diameter glass cylinder containing 1% intralipid was employed as the phantom, with an absorption coefficient of $\mu_a = 0.02 \text{ cm}^{-1}$ and a reduced scattering coefficient of $\mu'_s = 10.0 \text{ cm}^{-1}$. The cylinder was fixed on the rotation stage and the bottom was set to $Z = 0.0 \text{ cm}$. The quantification linearity of the system was validated by a transparent glass tube (0.4-cm diameter) containing fluorescent markers inserted into the cylinder. The tube was sequentially filled with different concentrations of ICG and corresponding FMT dataset was acquired subsequently. The experimental configuration is shown in Fig. 2a.

Average reconstructed fluorescence intensities were extracted from the region of interests (ROI) encompassing the fluorescent tube and then plotted as a function of actual ICG concentrations, as shown in Fig. 2b. The data demonstrates that the proposed system has a sensitivity of 13 nM concentration (260 fmole) of ICG and provides a good linear response from 13 nM to $3.25 \mu\text{M}$ of the fluorescent marker. Figure 2c depicts two cross section slices taken at the middle of the tubes, representing the reconstructed results of the lowest (13 nM) and highest ($3.25 \mu\text{M}$) ICG concentrations, respectively. Both tubes with a concentration difference of two orders of magnitude of ICG can be correctly localized.

Simultaneous Imaging Domain

Phantom experiment was performed to illustrate the area of simultaneous imaging domain on the imaged object. Two transparent glass tubes (0.4-cm diameter) were inserted into the cylinder with a vertical distance of 4.0 cm and horizontal distance of 1.5 cm, as shown in Fig. 3a. Each tube was filled with $1.3 \mu\text{M}$ ICG.

Figure 3 demonstrates the performance of the system for whole-body imaging of two fluorescent tubes placed at different positions in the phantom. As shown in Fig. 3b, both fluorescent targets were reconstructed simultaneously at the heights where the center of actual fluorescent tubes positioned ($Z = 1.4 \text{ cm}$ and $Z = 5.4 \text{ cm}$, respectively). The results suggest that both two tubes with a relatively large distance (4.3 cm

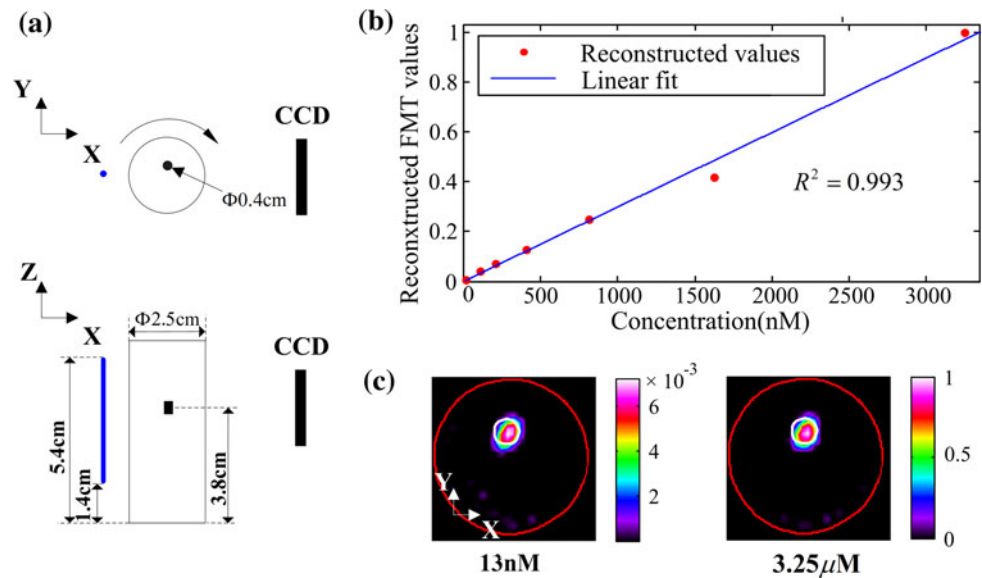


FIGURE 2. Phantom experiments for evaluating the quantification linearity of the system. (a) The top view and side view of the experimental configuration. A glass tube (0.4-cm diameter) sequentially filled with seven different concentrations (13 nM, 102 nM, 203 nM, 406 nM, 813 nM, 1.625 μ M, and 3.25 μ M) of ICG was inserted in a 2.5-cm diameter cylinder phantom. The *blue point* in the top view and the *blue line* in the side view both indicate the line-shaped parallel excitation source. (b) The average reconstructed fluorescence intensities as a function of actual ICG concentrations. *Blue solid line*, linear fit ($R^2 = 0.993$). (c) The reconstructed images corresponding to the lowest (13 nM) and highest (3.25 μ M) ICG concentrations, respectively, taken at slice $Z = 3.8$ cm. The reconstructed fluorescence intensities are normalized by the maximum of the reconstructed results. The *red curves* on the cross section images represent the phantom boundary, and the *small white circles* indicate the actual position of the tube.

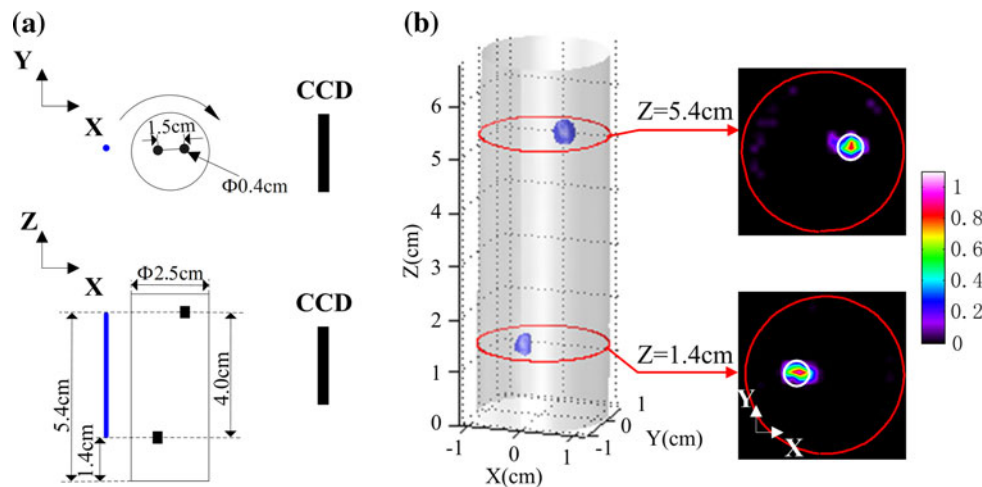


FIGURE 3. Phantom experiment for illustrating the simultaneous imaging domain of the system. (a) The top view and side view of the experimental configuration. Two glass tubes (0.4-cm diameter) filled with 1.3 μ M ICG were placed in a 2.5-cm diameter cylinder phantom at the height of 1.4 and 5.4 cm, respectively, with a horizontal distance of 1.5 cm. The *blue point* in the top view and the *blue line* in the side view both indicate the line-shaped parallel excitation source. (b) Reconstruction results of the two fluorescent tubes. Reconstructed fluorescence distributions are shown in the 3D view. The *red curves* on the cross section images represent the phantom boundary, and the *small white circles* represent the actual tube positions. Both images are normalized by the maximum of the reconstructed results and then displayed on the same color scale.

center-to-center distance) can be localized and quantified simultaneously during one full-angle FMT imaging process. Utilizing the line-shaped parallel excitation pattern, the system could achieve a simultaneous imaging domain of 4.0×1.5 cm² on the imaged object.

Whole-Body Simultaneous Imaging In Vivo

Animal experiment was also conducted to demonstrate the ability of this system in simultaneous imaging of the whole-body distribution of fluorescent markers *in vivo*. Two transparent glass bubbles (0.4-cm

diameter, 0.4-cm long) both filled with $1.3 \mu\text{M}$ ICG solution were implanted into a 6-week-old nude mouse by surgical incision through the abdominal wall. One bubble was positioned in the right upper abdomen while the other positioned in the left lower abdomen, in order to simulate the whole-body fluorescent marker distributions. After the mouse placed and fixed on the rotation stage, FMT data acquisition was performed. The mouse was anesthetized by isoflurane during the whole experimental process. The optical properties of $\mu_a = 0.3 \text{ cm}^{-1}$ and $\mu'_s = 10.0 \text{ cm}^{-1}$ were used for the *in vivo* FMT reconstruction.

Figure 4a depicts the white light image at angle 180° overlaid with the 4-cm long line-shaped parallel excitation beam and corresponding fluorescence image collected at the same angle. The upper two red dotted lines indicate the heights where the brightest fluorescence signals appeared. The two green arrows in the white light image indicate the surgical incisions through which the fluorescent bubbles were inserted.

As shown in Fig. 4b, both fluorescent targets were reconstructed around the heights where the brightest fluorescence signals appeared ($Z = 2.3 \text{ cm}$ and $Z = 0.8 \text{ cm}$, respectively). The positions of reconstructed targets were approximately in agreement with the bubble positions maintained in the experiment. The reconstructed results illustrate that both two bubbles

positioned at different regions of the mouse torso can be localized and quantified simultaneously during one full-angle FMT imaging process in *in vivo* experiment. As a result, based on the line-shaped parallel excitation pattern, whole-body FMT data acquisition time was reduced and the time resolution of imaging whole-body fluorescent marker distributions was improved.

DISCUSSION

Challenges remain in FMT imaging of complete dynamic physiological processes in small animals through the whole animal body, which boost the designing of imaging systems with a whole-body simultaneous imaging domain. Herein, we have presented a novel non-contact full-angle fluorescence tomography system for imaging the whole-body fluorescent marker distributions in small animals. The core element of the proposed system is a special optical fiber with one rectangular end, which is employed to generate a line-shaped parallel excitation pattern. The direct advantage gained by this parallel excitation pattern is the extended excitation domain on the imaged object, which is a necessity for whole-body simultaneous imaging. Both phantom and animal experiments were conducted to evaluate the performances of this system.

The quantitation linearity experiments demonstrated that the system can provide a highly linear response between reconstructed FMT intensities and actual fluorescent marker concentrations for over two orders of magnitude. It also showed that system has a sensitivity of 260 fmole of ICG.

A simultaneous imaging domain of $4.0 \times 1.5 \text{ cm}^2$ was observed in phantom experiment. It is acceptable considering the size of the mouse torso, which is the most commonly imaged object in FMT studies. Moreover, the imaging domain could be extended by lengthening the line-shaped parallel excitation fiber if necessary.

The performance of simultaneous imaging of whole-body distribution of fluorescent markers was validated *in vivo* by localizing and quantification two fluorescent targets placed at different positions of a nude mouse torso. Since the whole animal body of interest could be excited simultaneously and extended informative datasets to reconstruct multiple fluorescent targets distributed in the imaged object could be acquired at one full-angle FMT imaging process, whole-body FMT data acquisition time will be reduced. In our studies, the typical whole-body fluorescence signal acquisition time is $\sim 2 \text{ min}$, including the total exposure time and full-angle rotation time. Compared with our parallel excitation based system, conventional FMT

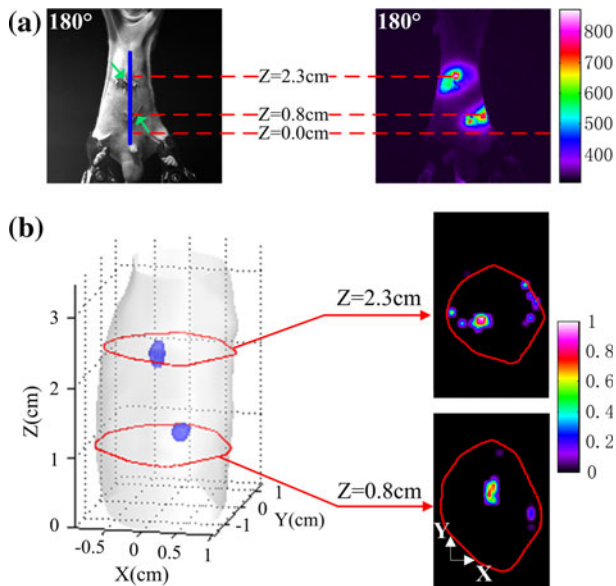


FIGURE 4. Whole-body simultaneous imaging of fluorescent bubbles *in vivo*. (a) The white light image overlaid with the 4-cm long line-shaped parallel excitation beam and corresponding fluorescence image collected at 180° . (b) Reconstruction results of the two fluorescent bubbles. Reconstructed fluorescence distributions are shown in the 3D view. The red curves on the cross section images represent the mouse surface. Both images are normalized by the maximum of the reconstructed results and then displayed on the same color scale.

systems with the single point excitation pattern could only excite a local region of the animal body. As a result, only fluorescent targets near the excitation point could be reconstructed correctly while other fluorescent targets are probably to be missed as they are relatively far from the excitation point. In order to obtain whole-body imaging results with the conventional single point excitation FMT system, the position of the excitation point should be changed successively to collect multiple cycles of projections. Consequently, the data acquisition time will be prolonged approximately linearly as the cycles of projection increased.³³ Thus, information loss is inevitable due to the lower sampling rate, which is unacceptable especially in imaging fast dynamic physiological processes *in vivo*. Therefore, the parallel excitation pattern of our system brings in an improved time resolution, which imparts the ability to capture the complete dynamic physiological processes with whole-body distribution of fluorescent markers *in vivo*.

Full-angle imaging results of the complete ICG whole-body metabolism process in nude mouse has already been acquired utilizing this system, as shown in Fig. 5. In practical cases, the mouse with fur can also be imaged except for nude mouse. However, the hair of the imaged region should be removed before imaging. For the hair removed mouse, similar imaging results were also obtained, although not shown in this article. Tomographic results of ICG metabolism process have not been provided in this article mainly due to two reasons. First, although the tomographic reconstruction was performed utilizing the normalized Born method, the influence of high optical property

heterogeneity in tissues could not be completely overcome, which may bring about error to the reconstructed results. Second, the accuracy of the reconstructed results could not be validated since the exact anatomical information of the internal tissues and organs in the mouse was unknown. Future work will be focused on resolving whole-body dynamic FMT images based on the principal component analysis (PCA) method,¹⁵ together with the aid of micro-computed tomography (micro-CT),³⁶ in order to improve the reconstruction quality¹² as well as to validate the accuracy of the reconstructed results.

In order to reduce the system complexity, the proposed system are implemented with the CCD camera and the excitation source fixed while the imaged mouse vertically suspended and rotated for full-angle FMT data acquisition. It is most practical from the physics point of view, and most of the reported non-contact full-angle FMT systems are constructed in this way.^{3,10,17} However, placing the mouse in a vertical position is not a pleasant way from the biological point of view. In a recently published hybrid FMT/X-ray computed tomography (XCT) system, the mouse was hold by two carbon rods in a horizontal position.²⁹ Similar system configuration could be referred in future system design to make the system more appropriate for biological application.

In conclusion, the full-angle FMT system based on a special line-shaped parallel excitation pattern presented here has direct advantage in the simultaneous imaging of whole-body fluorescence distributions during one full-angle FMT imaging process. Compared with conventional single point excitation FMT system, the

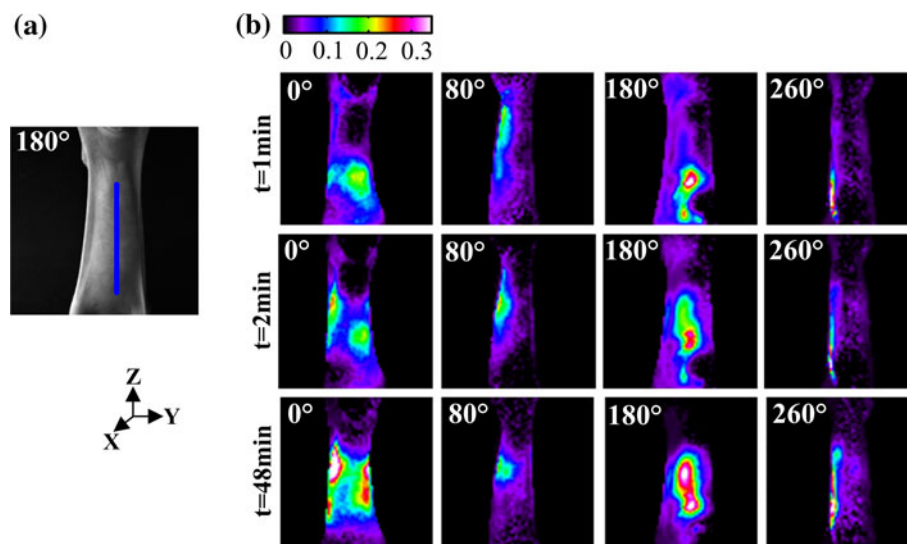


FIGURE 5. Full-angle whole-body imaging of ICG metabolism process *in vivo*. (a) The white light image overlaid with the 4-cm long line-shaped parallel excitation beam. (b) 0°, 80°, 180°, and 260° fluorescence imaging results of ICG distributions in a nude mouse acquired at different time points (1, 2, and 48 min) after tail vein injection. All the images are normalized by the maximum and then displayed on the same color scale.

proposed system with an extended imaging domain has an improved time resolution and consequently imparts the ability to capture the complete dynamic physiological processes in small animals. It provides an exciting application prospects in imaging whole-body dynamic physiological processes, such as disease progression, drug delivery, protein metabolism, etc.

ACKNOWLEDGMENTS

This work was supported by the National Natural Science Foundation of China under Grant No. 60831003, 30930092, 30872633; the Tsinghua-Yue-Yuen Medical Science Foundation; the National Basic Research Program of China (973) under Grant No. 2006CB705700; the National High-Tech Research and Development Program of China (863) under Grant No. 2006AA020803.

REFERENCES

- ¹Altinoğlu, E. I., T. J. Russin, J. M. Kaiser, B. M. Barth, P. C. Eklund, M. Kester, and J. H. Adair. Near-infrared emitting fluorophore-doped calcium phosphate nanoparticles for in vivo imaging of human breast cancer. *ACS Nano*. 2(10):2075–2084, 2008.
- ²Deliolanis, N. C., J. Dunham, T. Wurdinger, J. L. Figueiredo, T. Bakhos, and V. Ntziachristos. In vivo imaging of murine tumors using complete-angle projection fluorescence molecular tomography. *J. Biomed. Opt.* 14(3):030509, 2009.
- ³Deliolanis, N., T. Lasser, D. Hyde, A. Soubret, J. Ripoll, and V. Ntziachristos. Free-space fluorescence molecular tomography utilizing 360 degrees geometry projections. *Opt. Lett.* 32(4):382–384, 2007.
- ⁴Deliolanis, N., T. Lasser, M. Niedre, A. Soubret, and V. Ntziachristos. In vivo lung cancer imaging in mice using 360 degrees free-space fluorescence molecular tomography. *Conf. Proc. IEEE Eng. Med. Biol. Soc.* 1:2370–2372, 2006.
- ⁵Garofalakis, A., G. Zacharakis, H. Meyer, E. N. Economou, C. Mamalaki, J. Papamatheakis, D. Kioussis, V. Ntziachristos, and J. Ripoll. Three-dimensional in vivo imaging of green fluorescent protein-expressing T cells in mice with noncontact fluorescence molecular tomography. *Mol. Imaging* 6(2):96–107, 2007.
- ⁶Gotoh, K., T. Yamada, O. Ishikawa, H. Takahashi, H. Eguchi, M. Yano, H. Ohigashi, Y. Tomita, Y. Miyamoto, and S. Imaoka. A novel image-guided surgery of hepatocellular carcinoma by indocyanine green fluorescence imaging navigation. *J. Surg. Oncol.* 100(1):75–79, 2009.
- ⁷Graves, E. E., J. Ripoll, R. Weissleder, and V. Ntziachristos. A submillimeter resolution fluorescence molecular imaging system for small animal imaging. *Med. Phys.* 30(5):901–911, 2003.
- ⁸Graves, E. E., R. Weissleder, and V. Ntziachristos. Fluorescence molecular imaging of small animal tumor models. *Curr. Mol. Med.* 4(4):419–430, 2004.
- ⁹Haller, J., D. Hyde, N. Deliolanis, R. de Kleine, M. Niedre, and V. Ntziachristos. Visualization of pulmonary inflammation using noninvasive fluorescence molecular imaging. *J. Appl. Physiol.* 104(3):795–802, 2008.
- ¹⁰Hu, G., J. J. Yao, and J. Bai. Full-angle optical imaging of near-infrared fluorescent probes implanted in small animals. *Prog. Nat. Sci.* 18(6):707–711, 2008.
- ¹¹Hyde, D., R. de Kleine, S. A. MacLaurin, E. Miller, D. H. Brooks, T. Krucker, and V. Ntziachristos. Hybrid FMT-CT imaging of amyloid-beta plaques in a murine Alzheimer's disease model. *Neuroimage* 44(4):1304–1311, 2009.
- ¹²Hyde, D., E. L. Miller, D. H. Brooks, and V. Ntziachristos. Data specific spatially varying regularization for multimodal fluorescence molecular tomography. *IEEE Trans. Med. Imaging* 29(2):365–374, 2010.
- ¹³Joshi, A., W. Bangerth, and E. M. Sevick-Muraca. Adaptive finite element based tomography for fluorescence optical imaging in tissue. *Opt. Express* 12(22):5402–5417, 2004.
- ¹⁴Kitai, T., T. Inomoto, M. Miwa, and T. Shikayama. Fluorescence navigation with indocyanine green for detecting sentinel lymph nodes in breast cancer. *Breast Cancer* 12(3):211–215, 2005.
- ¹⁵Liu, X., D. Wang, F. Liu, and J. Bai. Principal component analysis of dynamic fluorescence diffuse optical tomography images. *Opt. Express* 18(6):6300–6314, 2010.
- ¹⁶Luker, G., and K. Luker. Optical imaging: current applications and future directions. *J. Nucl. Med.* 49(1):1–4, 2008.
- ¹⁷Meyer, H., A. Garofalakis, G. Zacharakis, S. Psycharakis, C. Mamalaki, D. Kioussis, E. N. Economou, V. Ntziachristos, and J. Ripoll. Noncontact optical imaging in mice with full angular coverage and automatic surface extraction. *Appl. Opt.* 46(17):3617–3627, 2007.
- ¹⁸Miyashiro, I., N. Miyoshi, M. Hiratsuka, K. Kishi, T. Yamada, M. Ohue, H. Ohigashi, M. Yano, O. Ishikawa, and S. Imaoka. Detection of sentinel node in gastric cancer surgery by indocyanine green fluorescence imaging: comparison with infrared imaging. *Ann. Surg. Oncol.* 15(6):1640–1643, 2008.
- ¹⁹Montet, X., J. L. Figueiredo, H. Alencar, V. Ntziachristos, U. Mahmood, and R. Weissleder. Tomographic fluorescence imaging of tumor vascular volume in mice. *Radiology* 242(3):751–758, 2007.
- ²⁰Montet, X., V. Ntziachristos, J. Grimm, and R. Weissleder. Tomographic fluorescence mapping of tumor targets. *Cancer Res.* 65(14):6330–6336, 2005.
- ²¹Ntziachristos, V. Fluorescence molecular imaging. *Annu. Rev. Biomed. Eng.* 8:1–33, 2006.
- ²²Ntziachristos, V., J. Ripoll, L. V. Wang, and R. Weissleder. Looking and listening to light: the evolution of whole-body photonic imaging. *Nat. Biotechnol.* 23(3):313–320, 2005.
- ²³Ntziachristos, V., E. A. Schellenberger, J. Ripoll, D. Yessayan, E. Graves, A. Bogdanov, L. Josephson, and R. Weissleder. Visualization of antitumor treatment by means of fluorescence molecular tomography with an annexin V-Cy5.5 conjugate. *Proc. Natl Acad. Sci. USA* 101(33):12294–12299, 2004.
- ²⁴Ntziachristos, V., C. H. Tung, C. Bremer, and R. Weissleder. Fluorescence molecular tomography resolves protease activity in vivo. *Nat. Med.* 8(7):757–760, 2002.
- ²⁵Ntziachristos, V., and R. Weissleder. Charge-coupled-device based scanner for tomography of fluorescent near-infrared probes in turbid media. *Med. Phys.* 29(5):803–809, 2002.
- ²⁶O'Leary, M. A., D. A. Boas, X. D. Li, B. Chance, and A. G. Yodh. Fluorescence lifetime imaging in turbid media. *Opt. Lett.* 21(2):158–160, 1996.

- ²⁷Patwardhan, S., S. Bloch, S. Achilefu, and J. Culver. Time-dependent whole-body fluorescence tomography of probe bio-distributions in mice. *Opt. Express* 13(7):2564–2577, 2005.
- ²⁸Rudin, M., and R. Weissleder. Molecular imaging in drug discovery and development. *Nat. Rev. Drug Discov.* 2(2):123–131, 2003.
- ²⁹Schulz, R. B., A. Ale, A. Sarantopoulos, M. Freyer, E. Soehngen, M. Zientkowska, and V. Ntziachristos. Hybrid system for simultaneous fluorescence and x-ray computed tomography. *IEEE Trans. Med. Imaging* 29(2):465–473, 2010.
- ³⁰Schweiger, M., S. R. Arridge, M. Hiraoka, and D. T. Delpy. The finite element method for the propagation of light in scattering media: boundary and source conditions. *Med. Phys.* 22(11):1779–1792, 1995.
- ³¹Song, X., D. Wang, N. Chen, J. Bai, and H. Wang. Reconstruction for free-space fluorescence tomography using a novel hybrid adaptive finite element algorithm. *Opt. Express* 15(26):18300–18317, 2007.
- ³²Soubret, A., J. Ripoll, and V. Ntziachristos. Accuracy of fluorescent tomography in the presence of heterogeneities: study of the normalized Born ratio. *IEEE Trans. Med. Imaging* 24(10):1377–1386, 2005.
- ³³Wang, D. F., X. Liu, and J. Bai. Analysis of fast full angle fluorescence diffuse optical tomography with beam-forming illumination. *Opt. Express* 17(24):21376–21395, 2009.
- ³⁴Wang, D. F., X. Liu, Y. Chen, and J. Bai. In vivo fluorescence molecular tomography based on optimal small animal surface reconstruction. *Chin. Opt. Lett.* 8(1):82–85, 2010.
- ³⁵Withrow, K. P., J. P. Gleysteen, A. Safavy, J. Skipper, R. A. Desmond, K. Zinn, and E. L. Rosenthal. Assessment of indocyanine green-labeled cetuximab to detect xenografted head and neck cancer cell lines. *Otolaryngol. Head Neck Surg.* 137(5):729–734, 2007.
- ³⁶Zhang, H., H. Li, G. Hu, G. S. Hu, and J. Bai. Micro-CT in a dual-modality fluorescence/computed tomography system for small animal imaging. *IEEE Nucl. Sci. Symp. Conf. Rec.* 3735–3737, 2007.